Received: 29 August 2022 | Revised: 19 October 2022 | Accepted: 20 October 2022

DOI: 10.1002/agt2.291

Aggregate WILEY Open Access

RESEARCH ARTICLE

Substituent-controlled aggregate luminescence: Computational unraveling of S_1/S_0 surface crossing

Ping-An Yin[1] | **Qi Ou**[1,2] | **Qian Peng**[3] | **Zhigang Shuai**[1,4]

[1]MOE Key Laboratory of Organic OptoElectronics and Molecular Engineering, Department of Chemistry, Tsinghua University, Beijing, China

[2]AI for Science Institute, Beijing, China

[3]School of Chemical Science, University of Chinese Academy of Sciences, Beijing, China

[4]School of Science and Engineering, The Chinese University of Hong Kong, Shenzhen, Guangdong, China

Correspondence
Qi Ou and Zhigang Shuai, MOE Key Laboratory of Organic OptoElectronics and Molecular Engineering, Department of Chemistry, Tsinghua University, 100084 Beijing, China.
Email: ouq@bjaisi.com; zgshuai@tsinghua.edu.cn

Funding information
National Natural Science Foundation of China, Grant/Award Numbers: 21788102, 2017YFA0204501

Abstract

We computationally investigated the molecular aggregation effects on the excited state deactivation processes by considering both the direct vibrational relaxation and the S_0/S_1 surface crossing, that is, the minimum energy conical intersection (MECI). Taking classical AIEgens bis(piperidyl)anthracenes (BPAs) isomers and the substituted silole derivatives as examples, we show that the deformation of MECI always occurs at the atom with greater hole/electron overlap. Besides, the energetic and structural changes of MECI caused by substituent has been investigated. We find that effective substituent such as the addition of the electron-donating groups, which can polarize the distribution of hole/electron density of molecules, will lead to the pyramidalization deformation of MECI occurring at the substituent position and simultaneously reduce the required energy to reach MECI. And MECI is sterically restricted by the surrounding molecules in solid phase, which remarkably hinders the non-radiative decay through surface crossing. Through quantitative computational assessments of the fluorescence quantum efficiency for both solution and solid phases, we elucidate the role of MECI and its dependence on the substitutions through pyramidalization deformation, which give rise to the aggregation-induced emission (AIE) phenomenon for 9,10-BPA, to aggregation-enhance emission (AEE) behavior for 1,4-BPA, and to conventional aggregation-caused quenching (ACQ) for 1,5-BPA. We further verify such mechanism for siloles, for which we found that the substitutions do not change the AIE behavior. Our findings render a general molecular design approach to manipulating the aggregation effect for optical emission.

KEYWORDS

aggregation-caused quenching, aggregation-induced emission, minimum energy conical intersection, substituent effect

1 | INTRODUCTION

Aggregation-induced emission (AIE) has become a hotspot research topic since the discovery by Tang et al.,[1,2] and substantial improvement of solid organic luminescence have been achieved.[3–6] Recent studies show that AIE molecules have been widely applied in photodynamic therapy,[7–9] luminescence probes for microbial detection,[10–12] and metal ion detection,[13,14] and ratiometric fluorescent sensor.[15] Many efforts have been devoted to qualitatively investigate the mechanism of the enhanced emission in the solid state,[16] such as earlier work by Oelkrug et al. on the role of head-to-tail alignment (J-aggregate) that redshifts the spectra and enhances fluorescence.[17] Recently, Tang et al. showed that intramolecular through-space interactions are essential.[18] One of the most widely approved AIE mechanisms is the restriction of the intramolecular motion (RIM) mechanism,[19–21] which includes the restriction of intramolecular rotation (RIR)[22] and the restriction of intramolecular vibration (RIV).[20] RIM serves a convenient way for an AIE molecule design, but related quantitative explanation is yet to be developed. Besides, the restriction of access to twisted intramolecular charge transfer (TICT) state that enables AIE of systems also attracts much attentions.[23,24]

Novel molecular design strategies are investigated on the basis of the aforementioned mechanisms to enrich the variety of aggregation-induced emission luminogens

(AIEgens).[24,25] Adding functional groups to classical AIE molecules such as tetraphenylethene (TPE) is a generally accepted strategy and has achieved great success in many reports.[26,27] Despite the rapid research development of AIE, applications of modification of simple core substrate to AIEgens are still hindered.[28] Recently, strategies that modify the potential energy surfaces (PES) of classical aromatic hydrocarbons such as naphthalene and anthracene to AIEgens attracted considerable attention.[29] Meanwhile, AIE design strategy that based on a conical intersection (CI) calculation, namely the control of conical intersection accessibility (CCIA), has achieved great success.[30] In 2015, 9,10-bis(piperidyl)anthracene (9,10-BPA) molecule was first reported by Konishi et al. as a new class of AIEgen.[31] And they have carried out computational investigations on a smaller systems (9,10-bis(dimethylamino)anthracene, 9,10-BDAAmethyl) to elucidate the fast internal conversion (IC) in solution of BPAs.[32] Despite the fact that experimental work claimed that the enhanced quantum yield of BPAs in the solid phase is contributed from slower non-radiative rates upon aggregation, as the low-lying minimum energy conical intersection (MECI) in solution rising much higher and become energetically inaccessible in the solid state, persuasive theoretical calculations and explanations of the substituent effect on the AIE phenomenon have not yet been performed. Indeed, the substituent effect is critically important for the photophysical behaviors, as shown in the cases of BPA by Konishi et al. that 9,10-BPA with typical AIE characteristic (the fluorescence quantum yield increase from 2.4% in toluene solution to 85.6% in solid phase), while 1,4-BPA with aggregation-enhance emission (AEE) as the fluorescence quantum yield slightly increases from 44.7% to 49.2%, and 1,5-BPA with aggregation-caused quenching (ACQ) characteristics with fluorescence quantum yield decrease from 58.8% to 34.4%, respectively.[31] In addition, the hypothesis of the substituent effect on the surface crossing through MECI is not clear. Even though it was suggested that AIEgen can be designed as long as the structure of the MECI is known,[33] we believe that a quantitative understanding on how the substituents affect the energy level of MECI as well as quantitative computation for the photophysical parameters remains a great challenging issue. In fact, the energetical and structural relationship between substituent and MECI has only been investigated for model molecules such as ethylene via on-the-fly nonadiabatic dynamics simulations.[34] Schuurman et al. revealed that the substituent group with greater π-electron donating/withdrawing abilities will lead to the decreasing of the energy required to reach MECI via the biradical model, while such algorithm is yet to be extended to realistic photoluminescent systems as the electronic structure of MECI is complicated. It is thus of great importance to quantitatively relate the substituent effect and the aggregate luminescence behaviors.

MECI structures for some AIEgens have been theorectially investigated previously,[35] and the restricted access to conical intersection (RACI) mechanism from solution to the solid phase for AIE is generally accepted.[36,37] Quantitative determination for the related decay rates remains unexplored, apart from femto-picosecond excited state dynamics simulations. Indeed, the explorations of the photo-physical properties especially the fluorescence emission efficiency Φ_{fl} are long-standing challenges in computational simulation. Computational challenge mainly lies in the fact that the radiative decay process is usually on the timescale of 10 ns, which is much slower than the time span of the best-available excited dynamic methods nowadays.[38–40] The non-radiative decay rate is even more challenging, as it varies in a wider range for pure organic dyes,[41–43] and becomes complicated in aggregates owning to the influence of the environment.[44,45] Rate formalism such as thermal vibration correlation function (TVCF) and transition state theory (TST) have been successively applied to circumvent these obstacles. Within the TVCF and TST rate formalisms, we have recently proposed a two-channel picture to quantitatively describe the decay process of the S_1 state and predict the quantum yield of boron dipyrromethene derivatives (BODIPYs) derivatives in solution,[46] with channel I the vibrational relaxation-induced non-radiative transition[47] and channel II the non-radiative decay through an S_0/S_1 MECI.[48]

2 | COMPUTATIONAL METHODOLOGY

The chemical structure of the investigated BPAs and silole derivatives are listed in Scheme 1. Geometries' optimizations of both S_0 and S_1 states as well as the S_0/S_1 MECI are performed via spin-flip time-dependent density functional theory (SF-TDDFT) method and def2-svp basis set. The SF-TDDFT method has become the method of choice for locating the S_0/S_1 MECI of medium- to large-size molecules owning to its low computational cost as well as the balanced and reliable description for both the ground and excited states. ωB97X-D functional is applied for all target molecules with an optimally tuned ω value for each system as shown in Table 1.[49] The choice of functionals relies on our benchmark results for the excitation energies listed in Table S2 (as compared to experimental absorption and emission spectra in Table S3). The solvent effect is addressed via the polarizable continuum model (PCM),[50] and the solid phase is modeled by a combined quantum-mechanical and molecular-mechanical (QM/MM)[51] method, and the electrostatic embedding scheme is applied in the QM/MM calculations. All of the electronic structure properties mentioned above are calculated in quantum chemistry package Q-chem 5.3.[52,53] The fluorescence spectra in both solution and solid phases are reproduced via our TVCF method as implemented in MOMAP program.[47,54,55] The hole–electron density analysis is performed base on Hirshfeld charge using the Multiwfn v3.5.1 software package.[56,57]

The optimized MECI structure of 9,10-bis (dimethylamino)anthracene (BDAA-methyl) is checked by comparing the computational results of SF-TDDFT with those of highly accurate correlation wavefunction method, that is, the complete active space self-consistent field (CASSCF).[32] The MECI structure of BDAA-methyl optimized by the two methods has the same structural characteristics as shown in Figure S1. As shown in Table S1, the computational result of the energy gap between Franck–Condon (FC)-S_1 and MECI is 0.43 eV by the SF-TDDFT method, which closely matches the computational result (0.46 eV) of the second-order multiconfigurational perturbation theory (CASPT2).

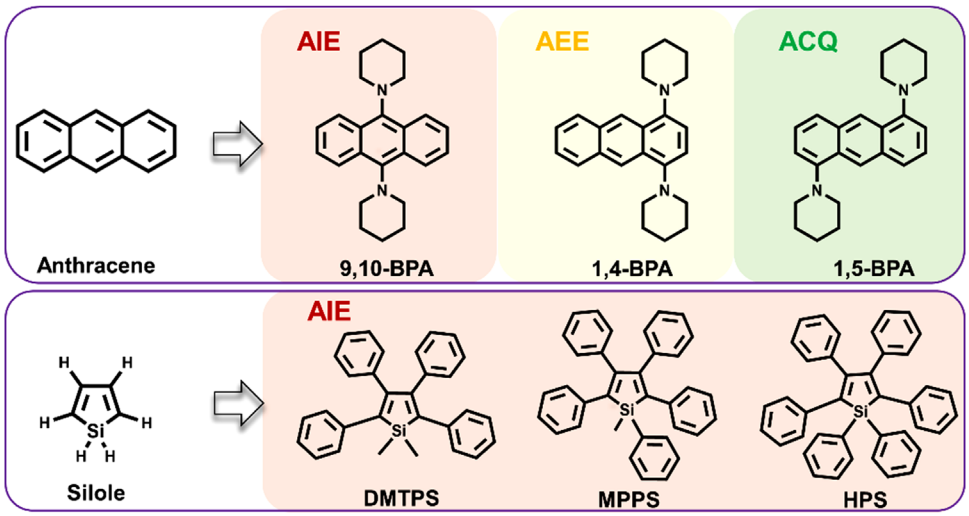

SCHEME 1 Chemical structures of the investigated BPAs and silole derivatives. The single-cystal materials of BPAs are from Ref. [31], the single crystal materials of silole derivatives are from Ref. [2]

TABLE 1 Computational vertical excitation energies at S_0 and S_1 optimized geometries of bis(piperidyl)anthracenes (BPAs) and silole derivatives

Molecule	State	Cal. Abs.(eV)	Exp. Abs.(eV)	Cal. Emi.(eV)	Exp. Emi.(eV)
9,10-BPA[a]	Toluene	2.99	3.00	2.39	2.29
	Solid	3.07	NA	2.41	2.31
1,4-BPA[b]	Toluene	3.04	3.08	2.14	2.11
	Solid	3.05	NA	2.24	2.03
1,5-BPA[c]	Toluene	3.26	3.08	2.74	2.45
	Solid	3.26	NA	2.74	2.32
DMTPS[d]	Cyclohexane	3.34	3.46	2.36	2.54
	Solid	3.33	3.41	2.36	2.70
MPPS[e]	Cyclohexane	3.26	3.42	2.25	2.49
	Solid	3.28	3.34	2.12	2.51
HPS[f]	Cyclohexane	3.11	3.42	2.23	2.49
	Solid	3.10	3.32	2.21	2.49

[a]Optimized by SF-TDDFT/ωb97X-D ($\omega = 0.157$)/Def2-SVP.
[b]Optimized by SF-TDDFT/ωb97X-D ($\omega = 0.167$)/Def2-SVP.
[c]Optimized by SF-TDDFT/ωb97X-D ($\omega = 0.172$)/Def2-SVP.
[d]Optimized by SF-TDDFT/ωb97X-D ($\omega = 0.135$)/Def2-SVP.
[e]Optimized by SF-TDDFT/ωb97X-D ($\omega = 0.124$)/Def2-SVP.
[f]Optimized by SF-TDDFT/ωb97X-D ($\omega = 0.121$)/Def2-SVP.

3 | RESULTS AND DISCUSSION

3.1 | Electronic structures and optical spectra

Konishi et al. demonstrated that the photophysical behaviors of three BPAs are significantly different, i.e., 9,10-BPA shows AIE characteristic as its fluorescence quantum yield increased from 2.4% to 85.6% from toluene solution to the solid state, while the 1,4-BPA manifests AEE phenomenon.[29] In contrast, 1,5-BPA exhibits ACQ, that is, the emission efficiency slightly decreases upon aggregation. We first compare the crystal packing patterns of all three BPA derivatives in Figure S2, where the experimental single crystal structures are also from Ref. [31]. It is seen that (i) the bulk density of crystals is different from each other, and the packing motif of 1,5-BPA crystal is not as compact as those of other two BPAs; (ii) the shortest intermolecular C–H distance among these BPAs is 2.785 Å in crystal of 1,5-BPA, which indicates that the intermolecular interactions are not expected to play a significant role in the luminescent properties of these crystalline structures. Therefore, the intermolecular interactions can be safely neglected in this work. Besides, as shown in Ref. [29], BPAs emit as a single molecule since their absorption/fluorescence spectral shapes in the solid phase are similar to that in the solution phase.

As listed in Table 1, vertical excitation energies predicted by aforementioned electronic structure methods are in good agreement with experimental observation. In addition, the spin contamination given by the SF-TDDFT method, which has long been questioned,[58] is not severe in this work according to the $\langle S^2 \rangle_{s_0}$ and $\langle S^2 \rangle_{s_1}$ values listed in Tables S2 and S3. Key geometric parameters of the computationally optimized ground state geometry in the solid state have

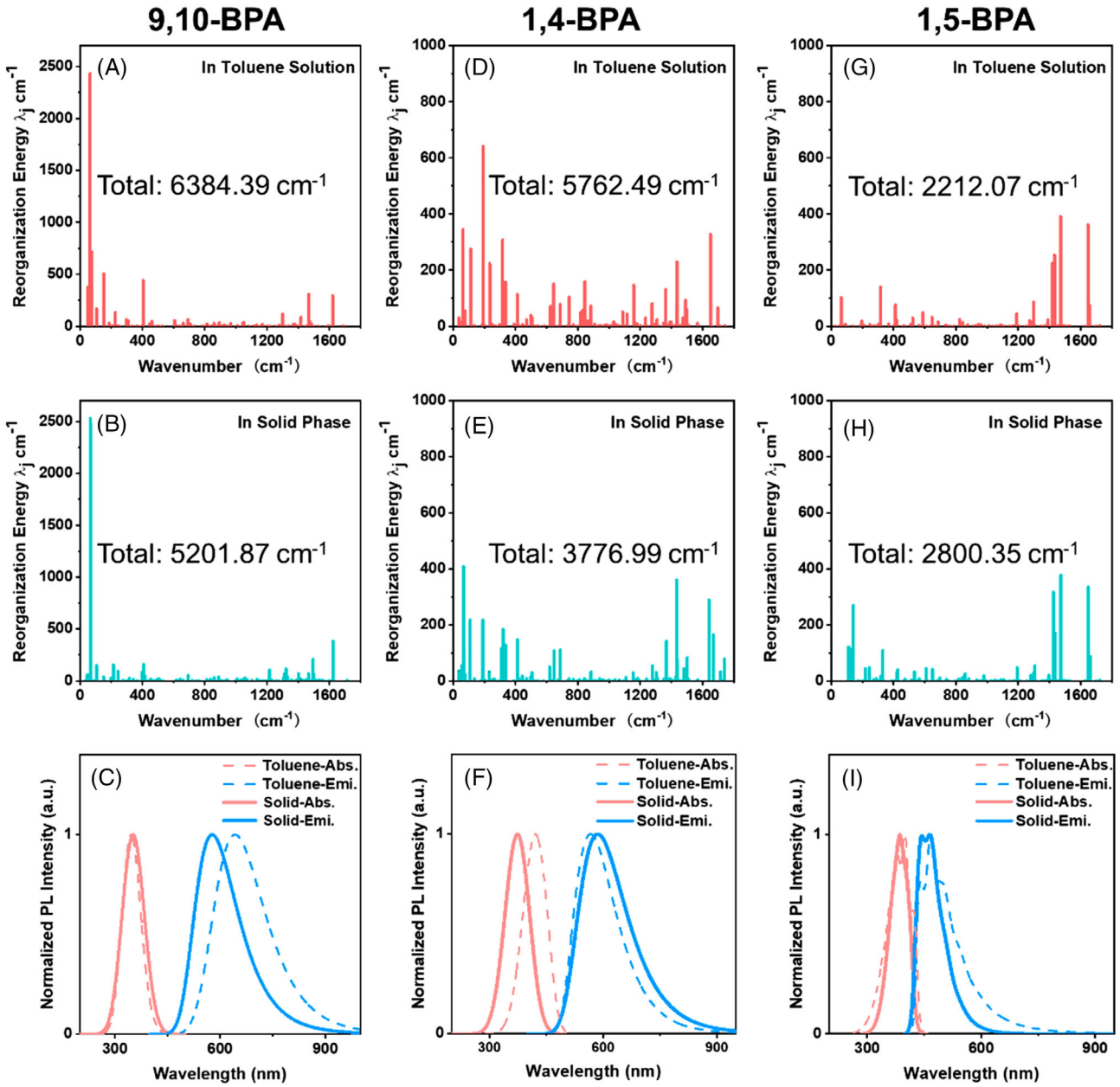

FIGURE 1 Reorganization energy and absorption and fluorescence spectra of bis(piperidyl)anthracenes (BPAs) in toluene solution and solid phase

been compared with the experimental crystal structure, taking 9,10-BPA as an example (Table S4; other optimized geometries are list in part 4 of Supporting Information). Despite a slight discrepancy on one piperidyl ring rotation along the C10–N2 single bond, the experimental structure of 9,10-BPA is perfectly recovered via aforementioned method. Details of the optimized geometries of other BPAs are listed in Supporting Information. In addition, we examine the existence of the TICT state in these BPAs by performing a relaxed scan of the PES for each dihedral angle between the piperidyl group and the plane of anthracene, from 90° to 180° with stepsize of 5°. The computational results show that the transition property of S_1 does not change with the dihedral angle (including excitation energy, oscillator strength, and frontier orbitals of S_1 in Figure S3), that is, no TICT formed during the rotation of the piperidyl group.

With the reliable electronic structure description, we are now ready to compute the fluorescence spectrum and quantum yield of BPAs. First, we investigate the fluorescence behavior of BPAs in both solution and the solid phase via TVCF methods. The calculated transition dipole moments (TDMs) of the investigated molecules at S_0 and S_1 states are listed in Tables S5 and S6. The computational absorption and fluorescence spectra in both solution and solid phases for BPAs are given in Figure 1. The calculated spectra are in line with the experimental counterparts from Ref.[31] in terms of the line-shape, the large Stokes shifts, and a broad full width at half-maximum (FWHM).

3.2 | Rate constants by thermal vibration correlation function

To quantitatively explore the excited state deactivation process in BPAs, we calculate the radiative rates k_r and non-radiative rates k_{nr} of the S_1 state. The radiative rate of

TABLE 2 Computational rate constants of k_r^{TVCF} and k_{nr}^{TVCF} (channel I) and k_{nr}^{MECI} (channel II) and fluorescence quantum yield Φ_{fl}^{cal} of target bis(piperidyl)anthracenes (BPAs) and silole derivatives

Molecule	State	k_r^{TVCF} (10^8 s^{-1})	k_{nr}^{TVCF} (10^8 s^{-1})	$\Delta G^{\neq}$ (kcal/mol)	k_{nr}^{MECI}(s^{-1})	Φ_{fl}^{cal}	Φ_{fl}^{exp}
9,10-BPA	Toluene	0.42	0.23	4.20 (TS)	5.18×10^9	0.80%	2.4%
	Solid	0.57	0.50	21.95	4.91×10^{-4}	53.3%	85.6%
1,4-BPA	Toluene	0.28	1.98	14.01	3.27×10^2	12.5%	44.7%
	Solid	0.39	0.27	34.31	4.23×10^{-13}	59.1%	49.2%
1,5-BPA	Toluene	0.96	0.46	30.43	3.00×10^{-10}	67.6%	58.8%
	Solid	1.17	0.37	49.30	4.28×10^{-24}	76.0%	34.4%
DMTPS	Cyclohexane	0.75	5.99	1.84	2.76×10^{11}	0.03%	0.22%
MPPS	Cyclohexane	0.79	32.8	4.26 (TS)	4.64×10^9	0.99%	0.13%
HPS	Cyclohexane	0.55	6.43	4.75 (TS)	2.03×10^9	2.0%	0.30%

the S_1 state can be calculated as the integration of the light emission spectrum via the TVCF method:

$$k_r^{TVCF} = \int_0^{\infty} \sigma_{em}(\omega)\, d\omega, \tag{1}$$

where the emission spectrum function

$$\sigma_{em}(\omega) = \frac{4\omega^3}{3c^3} \sum_{\nu_i,\nu_f} P_{i\nu_i}(T) \left| \langle \Theta_{f\nu_f} | \vec{\mu}_{fi} | \Theta_{i\nu_i} \rangle \right|^2 \times \delta\left(E_{if} + E_{i\nu_i} - E_{f\nu_f} - \hbar\omega\right), \tag{2}$$

where c is the velocity of light, $P_{i\nu_i}(T)$ is the Boltzmann distribution function for initial vibronic manifold, $\vec{\mu_{fi}}$ is the electric TDM, E_{if} represents the adiabatic excitation energy, $E_{i\nu_i}$ ($E_{f\nu_f}$) is the vibrational energy in the initial (final) electronic state. The nonradiative decay process of the S_1 state contains two paths, that is, IC via vibrational relaxation (channel I) to S_0 and intersystem crossing (ISC) to T_n. Here, we neglect the influence of ISC due to the fact that for all investigated molecules, no phosphorescence was found experimentally.[29] The rate constant of the nonradiative decay process k_{nr} can therefore be approximately considered as the IC rate constant as:

$$k_{nr} = \frac{1}{\hbar^2} R_{kl} \int_{-\infty}^{\infty} dt \left[e^{i\omega_{if}t} Z_i^{-1}(t,T)\, \rho_{ic,kl}(t,T) \right], \tag{3}$$

where $\rho_{ic,kl}(t,T)$ is the IC TVCF.

The fluorescent efficiency can be easily evaluated as:

$$fl_{fl} = \frac{k_r}{k_r + k_{nr}}. \tag{4}$$

The calculated excited state decay rates for various substituted BPAs and siloles' derivatives in both solution and solid phases are listed in Table 2. The theoretical fluorescent efficiencies of target molecules with strong emission are in good agreement of the experimental data in both solid and solution phases, while the quantum efficiencies calculated for the weak fluorescent emitters are severely overestimated, which indicates that considering only vibrational relaxation (channel I) via TVCF is not sufficient for qualitative prediction on the photoluminescence quantum yield (PLQY). It should be borne in mind that for systems of which the AIE phenomena can be accurately described via TVCF, for example, the metal complexes,[59] the property of S_1 in solution is quite different from that of the solid state; its large reorganization energies are mainly contributed from the low-frequency modes in solution, while these modes can be remarkably suppressed in the solid phase, and therefore the decay rate via direct vibrational relaxation (channel I) is significantly decreased from solution to the solid phase. In contrast, S_1 for BPAs in the solution phase is quite similar in nature to the solid phase, and hence the change of decay rates in the harmonic region is not significant upon aggregation. Thus, to account for the AIE phenomena in BPAs, it is necessary to consider the contributions from the restriction of decay path through an S_0/S_1–MECI in the solid phase.[60]

The electronic structure for the first excited state in solution is quite similar to that for the solid phase as demonstrated by the calculated reorganization energy. As shown in Figure 1, the reorganization energy of 9,10-BPA slightly decreases from 6384 to 5202 cm^{-1} from the solution phase to the solid phase due to a more rigid environment upon aggregation. Similar trend is observed for 1,4-BPA. For 1,5-BPA, the reorganization energy tends to increase from 2212 cm^{-1} in solution to 2800 cm^{-1} in the solid phase. It is obvious that the contribution of low-frequency normal modes in 1,5-BPA system is significantly smaller than those of the other two systems both in solution and the solid phase, indicating that this molecule is more rigid than other investigated molecules. Altogether, these findings prove that the AIE phenomena of 9,10-BPA are not only led by the restriction of the low-frequency modes upon aggregation, and the effect of channel II has to be taken into consideration.

3.3 | Minimum energy conical intersection and substituent effect

To quantitatively unravel the AIE/ACQ mechanisms, we further investigate the S_0/S_1 MECI for all BPAs in both toluene solution and solid phase (Figure S4). The computational MECI structure and relative energies of target molecules are shown in Figure 2. The deformation of 9,10-BPA and

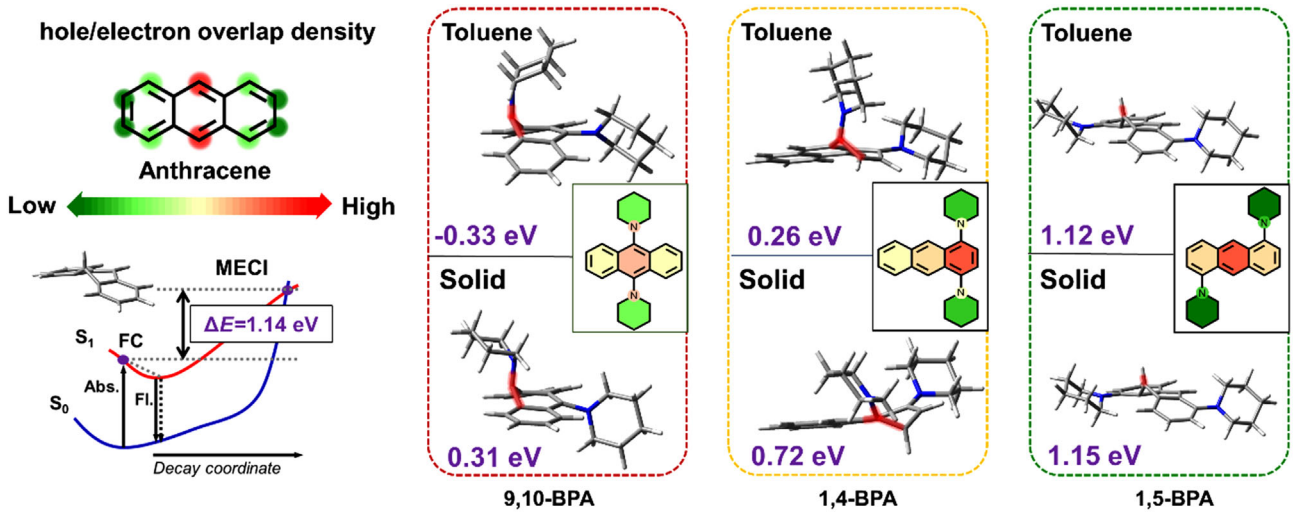

FIGURE 2 Minimum energy conical intersection (MECI) structure and the energy gap between Franck–Condon (FC) and MECI of anthracene (toluene) and bis(piperidyl)anthracenes (BPAs)

1,4-BPA mainly arises from the out-of-plane reversal of the piperidyl ring along the C–N bond, while the MECI structure of 1,5-BPA deforms as its C–H bond at 9-positions upward. The relative energy gap between FC structure and MECI drastically varies with respect to the positions of two piperidyl rings. In 9,10-BPA, the energy gap between FC and MECI structure (ΔE) is −0.33 eV in toluene solution and 0.31 eV in the solid phase. The ΔE of 1,4-BPA is 0.26 eV in solution and increase to 0.72 eV in the solid phase, while it becomes significantly larger of 1,5-BPA (1.12 and 1.15 eV in solution and solid phase, respectively). It is obvious that the energy required to reach MECI of BPAs and anthracene in the solid phase becomes higher than that in the solution phase, as the steric hinderance effect and electrostatic interaction from surrounding molecules in the solid phase make the pyramidalization deformation of MECI energetically unaccessible. The trend in energy gaps between FC point and MECI of these three BPAs evidences that introducing piperidyl at C9, C10 and C1, C4 position makes the MECI more energetically accessible. To further reveal the relationship between such substituent effect and the MECI energy, we investigate the characteristics of MECI of anthracene. As shown in Figures 2 and S5, the MECI geometry of anthracene puckers at C9 position, and its ΔE is 1.14 eV in toluene solution and increases to 1.57 eV in the solid phase, which is significantly higher than that of 9,10-BPA and 1,4-BPA. It is clear that the piperidyl substituent of anthracene will lead to energetically lower MECI. To explore the inherent relationship between substituent position and the structural and energetical trends of MECI of BPAs, we investigate hole–electron overlap distribution density of S_0-min for all BPAs in both solution and solid phases, as well as that for anthracene for comparison. As shown in Figure 3 and Table S7, nearly 14% hole–electron overlap density of anthracene distributes at C9 and C10 positions, and such distribution decreases to 7.5% at C1 position and 5% at position C2. (Positions that are not available for substituent are neglected.) The distribution of hole–electron density and the hole–electron overlap for anthracene in solid is similar to that in the gas phase. Distribution of hole–electron overlap density in 1,5-BPA is similar to that of anthracene, which leads to the fact that pyramidalization deformation of MECI in 1,5-BPA appears in the same position (C9) as anthracene with closely matched ΔE as compared to anthracene. For 9,10-BPA, the distribution of hole is mainly located at N1 and N2 (nearly 15%) in toluene solution, while the distribution of hole is located at N1 (27%) in the solid phase as symmetry broken (as shown in Figure S6). Though the highest hole–electron overlap still located at 9,10-position, it decreases to 9% in both solution and solid phase. Contrarily, for 1,4-BPA, the hole–electron overlap density evenly distributes at four positions (8% for C9, C10, C1, and C4). Besides, the deformation of the MECI structure appears at position C1. What can be drawn from these observations is that atoms with the greater hole–electron overlap density are prone to possess pyramidalization motions. Moreover, the effective substituent like the electron donating groups (piperidyl), which significantly change the hole and electron density distribution of unsubstituted molecule, will lead to different hole-electron overlap distribution, and reduce the energy required to reach the MECI structure compare to the unsubstituted molecule (as shown in Table S8). It is worth mentioning that experimental studies are consistent with our conclusions here. Ref. [31] shows that the single substituent (piperidyl) at positions C1, C2, C9 leads to different photophysical behaviors in solution. 1-PA and 2-PA exhibit strong fluorescence in solution, while 9-PA barely fluoresces in solution. According to aforementioned discussion, the reason for such phenomenon is that piperidyl substituent at position C9 significantly alters the hole–electron overlap density and lowers the MECI energy in solutions. Contrarily, significant change on the hole–electron overlap density is not observed for piperidyl substituent at C1 and C2, and hence the MECI of 1-PA and 2-PA are similar to anthracene and which is energetically inaccessible even in the solution phase.

3.4 | Two-channel model for nonradiative decay

In our previously proposed two-channel scheme, the total k_{nr} should be calculated as $k_{nr} = k_{nr}^{TVCF} + k_{nr}^{MECI}$, where k_{nr}^{TVCF} and k_{nr}^{MECI} represent the two nonradiative decay rates from different channels. The TST has been introduced to

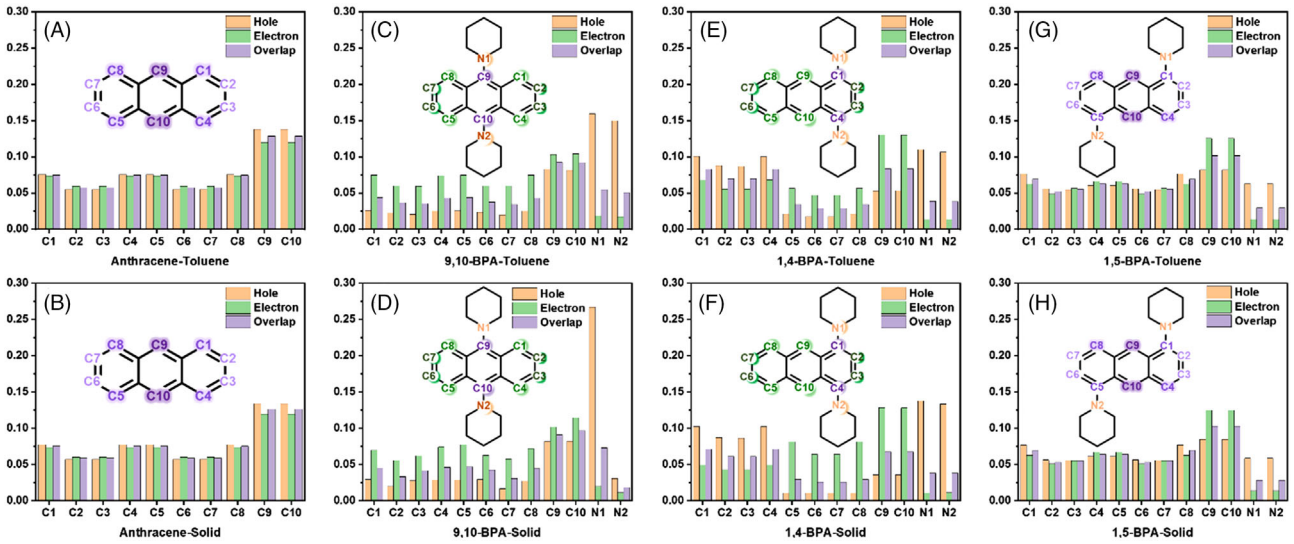

FIGURE 3 Hole/electron density and the hole–electron overlap distribution for anthracene and bis(piperidyl)anthracenes (BPAs) in solution and solid phases

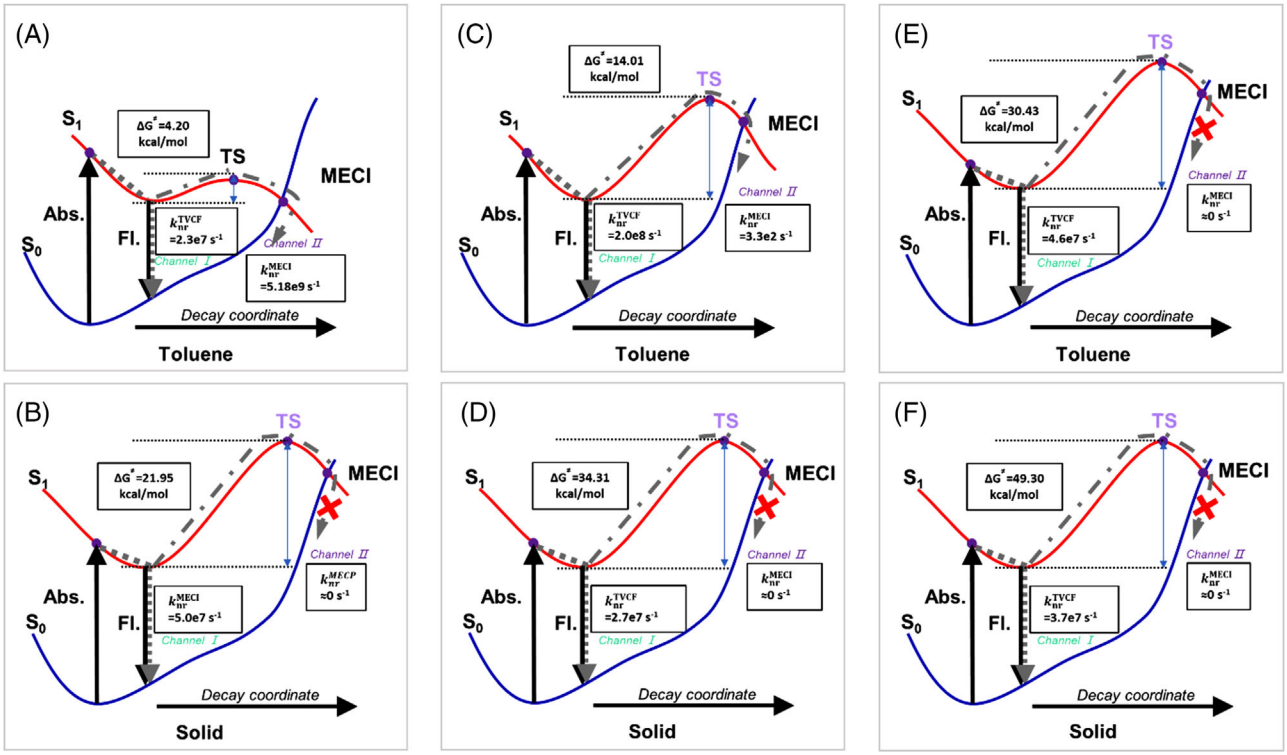

FIGURE 4 Schematic graph of the two nonradiative decay channels for 9,10-bis(piperidyl)anthracene (BPA) (A) in toluene solution; (B) in solid phase; 1,4-BPA (C) in DMF solution; (D) in solid phase; 1,5-BPA (E) in toluene solution; (F) in solid phase

quantitatively describe the influence of channel II as

$$k_{\mathrm{nr}}^{\mathrm{MECI}} = \frac{k_{\mathrm{B}}T}{h}\exp\left(-\frac{\Delta G^{\neq}}{RT}\right), \tag{5}$$

where $\Delta G^{\neq}$ is the Gibbs free energy of activation between the S_1-min structure and the high-lying transition state (TS) structure (higher in energy than MECI) along the reaction path. To compute $\Delta G^{\neq}$, we choose the thermodynamic data at the stationary structure (S_1-min) and that at TS/MECI. The computed value of $\Delta G^{\neq}$ and $k_{\mathrm{nr}}^{\mathrm{MECI}}$ are indicated in Figure 4 and Table 2, where TS shown in purple indicates that no TS lower than MECI could be found. Low-lying MECIs have been located for 9,10-BPA in toluene. In practice, we started with the low-lying MECIs structure as the initial guess to search the minimum S_0, and we found that it always comes back to the original structure, instead of the photo-productant structure. The MECI energies in other cases are much higher than the energies of FC structures, as shown in Figure 3, which means that the contribution of channel II is negligible in such cases due to the large energy gap. For 9,10-BPA, the energy of the TS structure in toluene solution is lower than the energy of the FC structure. The energy gap between S_1-min and TS is 0.22 eV, and the corresponding

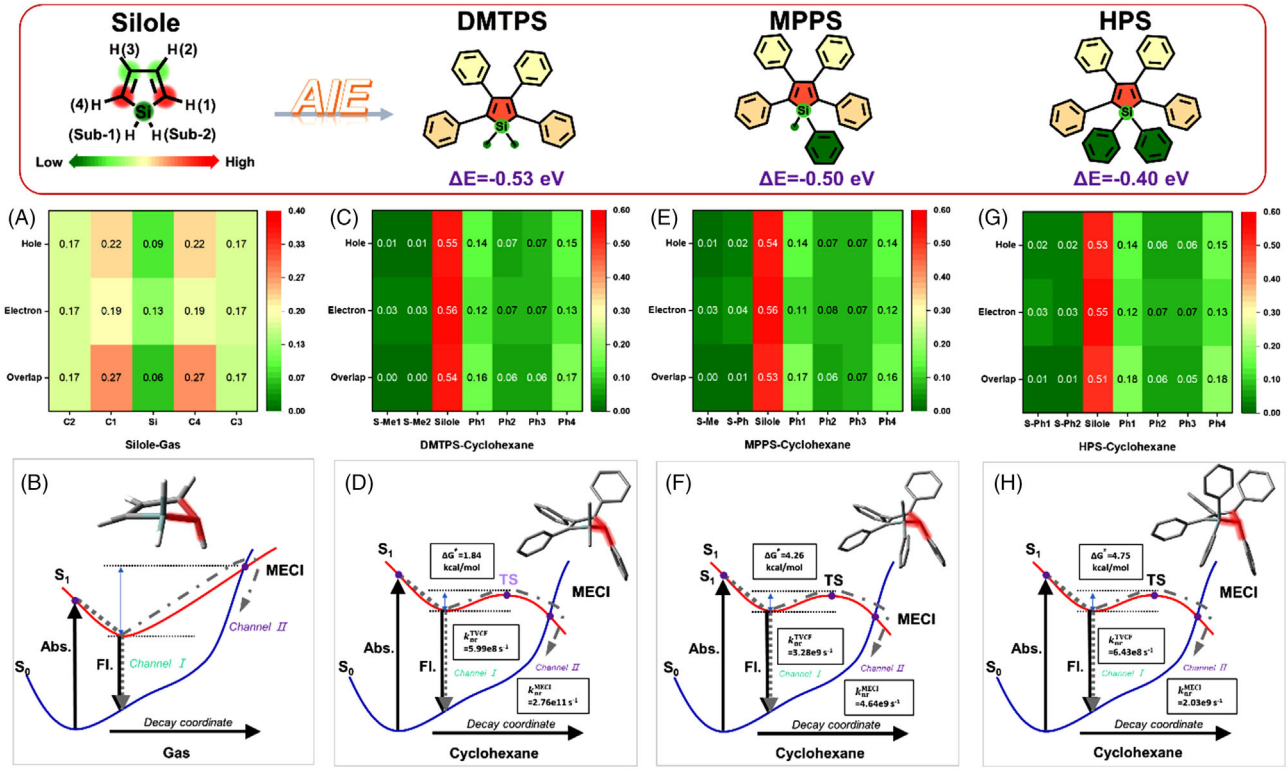

FIGURE 5 Heat map of hole/electron and the hole–electron overlap density and schematic graph of the two non-radiative decay channels of (A,B) silole; (C,D) DMTPS; (E,F) MPPS; (G,H) HPS in cyclohexane solution

$\Delta G^{\neq}$ is 4.32 kcal/mol, and the corresponding $k_{nr}^{MECI} = 4.22 \times 10^9$ s^{-1} is 2 orders of magnitude larger than k_{nr}^{TVCF}. Thus, the inclusion of k_{nr}^{MECI} can significantly modify the total rate constant of nonradiative process, and a more reasonable fluorescent efficiency $fl_{fl}^{corr} = 0.80\%$ (experimental results is 2.4%) can thus be obtained. The energy of MECI is 0.69 eV higher than the energy of S_1-min structure in solid phase, and k_{nr}^{MECI} thus becomes negligible and the contribution of channel II can be ignored upon aggregation. Based on these theoretical findings, the enhanced fluorescence efficiency from solution to the solid phase of 9,10-BPA can be attributed to the restriction of the nonradiative process through channel II. For 1,4- and 1,5-BPA, which exhibit AEE and ACQ behaviors, respectively, the computational results indicate that the high fluorescence efficiency of these two molecules in solution is also attributed to an energetically higher MECI in channel II (as shown in Figure 1) compared to the case of 9-10 BPA. These computational results further validate that the substitution by electron donating groups at positions with high hole–electron overlap density could reduce the energy required to reach S_0/S_1 MECI, leading to fast decay of the S_1 through channel II.

3.5 | Minimum energy conical intersection of silole derivatives

Finally, we apply the two-channel framework for the nonradiative decay process to quantitatively calculate the photo-physical properties of a serials of silole derivatives, 1,1-dimethyl-2,3,4,5-tetraphenylsilole (DMTPS), 1-methyl-1,2,3,4,5-pentaphenylsilole (MPPS) and 1,1,2,3,4,5-hexaphenylsilole (HPS), the classical AIEgens. The calculated spectra of absorption and emission are presented in Figure S7, along with the analysis of the hole–electron overlap density and ΔE. It was found that only one type of minimum energy MECI for siloles, namely, the puckered carbon atom bonded to silicon.[61] It is in line with the previous investigations on the propeller-shaped molecules such as 1,2,3,4-tetraphenyl-1,3-cyclopentadiene.[62–64] We optimize the minimum S_0/S_1 MECI structure and analyze its hole–electron overlap density, as shown in Figure 5 and Table S9. The latter distributes mainly at the C1/C4 bonded to silicon (27%), and about 17% at the other two carbon atoms and only 6% at silicon atom. The S_0/S_1 MECI structure of silole obeys the rule that the deformation of MECI tends to occur at the atom with greater hole–electron overlap density.[61] After the substitution by phenyl at positions C1, C2, C3, and C4, the hole and electron density moves to the phenyl at positions C1 and C4, while the distribution of hole–electron overlap density of the substituent group at silicon barely changes. As shown in Figure 5B–D, we examine seven different fragments of the derivatives, and find that the hole–electron overlap density mainly distributes at the silole ring (>50%) and at the Ph1 and Ph4 groups (>15%). Thus, in consistent with the rule we proposed above, the phenyl substituent at positions C1 and C4 will reduce the energy gap required to reach the MECI of silole derivatives and result in smaller ΔE compare to silole. Moreover, the MECI structure of silole derivatives is prone to pyramidalization at C1 or C4. The non-radiative decay paths of silole derivatives in cyclohexane are also investigate by the two-channel scheme. As shown in Table 2, considering only the computational decay path in the harmonic region will overestimate the quantum yield of these systems. It is obvious that the deactivation through channel II is not negligible as the substituent effect polarizes the hole

and electron density and results in the energetically low-lying MECI of these derivatives in solution. The energy of the TS structure of MPPS and HPS in cyclohexane solution is lower than the energy of FC structure, which is visualized in Figure 5. The energy gap between FC and MECI is −0.53, −0.52, and −0.40 eV. The $\Delta G^{\neq}$ between S_1-min and MECI/TS is 1.84, 4.26, and 4.75 kcal/mol, respectively. Details of the thermodynamic data can be found in Table S10. Thus, the decay path through channel II becomes important in solution for these silole derivatives, while it can be ignored after aggregation since the large-amplitude pyramidalization motions are restricted by surrounding molecules (which has been qualitatively discussed in Ref. [37]).

4 | CONCLUSION

To conclude, we have calculated the photophysical parameters for BPA and silole derivatives in both solution and solid phases employing a two-channel model for the excited state non-radiative decay considering both the vibrational relaxation and S_1/S_0 surface crossing. We first benchmarked the starting electronic structure calculation. We find that the calculated electronic structures at the SF-TDDFT/ωB97X-D/def2-svp level are in good agreement with the experimental results. And the fluorescence spectra in both solution and solid phases have been successfully reproduced via our TVCF method as implemented in MOMAP program. A wide range of photophysical behaviors from ACQ, AEE to AIE phenomenon, can be quantitatively described at the same footings. Theoretical findings evince that MECI is essential for the aggregation effect and can be controlled by substituents. MECIs for 9,10-BPA and 1,4-BPA are more accessible than that of 1,5-BPA. In the former cases, the pyramidalization deformation of MECI occurs at the substituent position, leading to an energetically lower lying MECI compared to other BPAs in solution, while such prominent pyramidalization motions of the large-sized substituent group is found to be restricted upon aggregation, leading to strong optical emission in the solid phase (AIE). The MECI structure of 1,4-BPA has the same structural characteristics as 9,10-BPA, with deformation mainly arising from the out-of-plane reversal of the piperidyl ring along the C–N bond. However, the energy required to reach MECI in 1,4-BPA becomes higher than that of 9,10-BPA in both solution and solid phases. The reduced non-radiative decay rates through channel II lead to the higher PLQY in solution, manifesting an AEE behavior. For 1,5-BPA, the deformation of MECI occurs at the C9 position instead of the substituent position, which maintain the same structural and energetical characteristics as the unsubstituted, the typical ACQ chromophore. Namely, the MECI of 1,5-BPA is energetically unaccessible in both solution and solid phases. Besides, the pyramidalization deformation of MECI in BPAs tends to occur at the atomic site with greater hole−electron overlap density in both solution and solid phases. Only when the substituent effectively polarizes the hole and electron density distribution to a noticeable extent for pyramidalization deformation, can MECI occur at the substituent position with an energetically lower level. We find that this rule is also applicable to explain the classical AIEgens like silole and its substituted derivatives. Looking forward, the quantitative photophysical simulation of target molecules we have made here gives a novel and quantitative perspective to understand the AIE phenomenon and can be easily applied to other AIEgens. The relationship of the substituent effect on the energetical and structural influence of S_0/S_1 MECI we revealed here may help the design of new AIEgens.

ACKNOWLEDGEMENTS

This work is supported by the National Natural Science Foundation of China through the Science CEnter for Luminescence from Molecular Aggregates (SCELMA) project (Grant 21788102) and the Ministry of Science and Technology of China (Grant 2017YFA0204501). We gratefully acknowledge HZWTECH for providing computation facilities.

CONFLICT OF INTEREST

The authors declare that there is no conflict of interest that could be perceived as prejudicing the impartiality of the research reported.

ORCID

Qian Peng https://orcid.org/0000-0001-8975-8413
Zhigang Shuai https://orcid.org/0000-0003-3867-2331

REFERENCES

1. J. Mei, Y. Hong, J. W. Y. Lam, A. Qin, Y. Tang, B. Z. Tang, *Adv. Mater.* **2014**, *26*, 5429.
2. J. Luo, Z. Xie, J. W. Y. Lam., L. Cheng, H. Chen, C. Qiu, H. S. Kwok, X. Zhan, Y. Liu, D. Zhu, B. Z. Tang, *Chem. Commun.* **2001**, *37*, 1740.
3. X. Cai, B. Liu, *Angew. Chem. Int. Ed.* **2020**, *59*, 9868.
4. Z. Zhao, J. W. Y. Lam, B. Z. Tang, *J. Mater. Chem.* **2012**, *22*, 23726.
5. W. Z. Yuan, Y. Gong, S. Chen, X. Y. Shen, J. W. Y. Lam, P. Lu, Y. Lu, Z. Wang, R. Hu, N. Xie, H. S. Kwok, Y. Zhang, J. Z. Sun, B. Z. Tang, *Chem. Mater.* **2012**, *24*, 1518.
6. S. Fery-Forgues, C. Vanucci-Bacqué, *Topics Curr. Chem.* **2021**, *379*, 32.
7. S. Wang, X. Wang, L. Yu, M. Sun, *Photodiagnosis Photodyn*. **2021**, *34*, 102254.
8. J. Li, Z. Zhuang, Z. Zhao, B. Z. Tang, *View* **2022**, *3*, 20200121.
9. W. Wu, Z. Li, *Mater. Chem. Front.* **2021**, *5*, 603.
10. S. Chen, R. Luo, X. Li, M. He, S. Fu, J. Xu, *Materials* **2021**, *14*, 1909.
11. H. Tian, A. C. Sedgwick, H.-H. Han, S. Sen, G.-R. Chen, Y. Zang, J. L. Sessler, T. D. James, J. Li, X.-P. He, *Coord. Chem. Rev.* **2021**, *427*, 213577.
12. N. Rohaizad, C. C. Mayorga-Martinez, M. Fojtů, N. M. Latiff, M. Pumera, *Chem. Soc. Rev.* **2021**, *50*, 619.
13. P. Alam, N. L. C. Leung, J. Zhang, R. T. K. Kwok, J. W. Y. Lam, B. Z. Tang, *Coord. Chem. Rev.* **2021**, *429*, 213693.
14. Y. Li, H. Zhong, Y. Huang, R. Zhao, *Molecules* **2019**, *24*, 4593.
15. Y. Yuan, D. Wang, W. Long, F. Deng, S. Yu, J. Tian, H. Ouyang, S. Lin, X. Zhang, Y. Wei, *Sens. Actuators B Chem.* **2021**, *330*, 129324.
16. Q. Peng, Z. Shuai, *Aggregate* **2021**, *2*, e91.
17. D. Oelkrug, A. Tompert, J. Gierschner, H.-J. Egelhaaf, M. Hanack, M. Hohloch, E. Steinhuber, *J. Phys. Chem. B* **1998**, *102*, 1902.
18. J. Liu, H. Zhang, L. Hu, J. Wang, J. W. Y. Lam, L. Blancafort, B. Z. Tang, *J. Am. Chem. Soc.* **2022**, *144*, 7901.
19. D. Tu, J. Zhang, Y. Zhang, H. H. Y. Sung, L. Liu, R. T. K. Kwok, J. W. Y. Lam, I. D. Williams, H. Yan, B. Z. Tang, *J. Am. Chem. Soc.* **2021**, *143*, 11820.
20. N. L. C. Leung, N. Xie, W. Yuan, Y. Liu, Q. Wu, Q. Peng, Q. Miao, J. W. Y. Lam, B. Z. Tang, *Chem. Eur. J.* **2014**, *20*, 15349.
21. Z. Zhao, H. Zhang, J. W. Y. Lam, B. Z. Tang, **2020**, *Angew. Chem. Int. Ed. 59*, 9888.
22. Y. Hong, J. W. Y. Lam, B. Z. Tang, *Chem. Commun.* **2009**, *45*, 4332.
23. S. A. A. Abedi, W. Chi, D. Tan, T. Shen, C. Wang, E. C. X. Ang, C.-H. Tan, F. Anariba, X. Liu, *J. Phys. Chem. A* **2021**, *125*, 8397.
24. W. Yu, H. Zhang, P.-A. Yin, F. Zhou, Z. Wang, W. Wu, Q. Peng, H. Jiang, B. Z. Tang, *iScience* **2020**, *23*, 101587.
25. S. Choi, J. Bouffard, Y. Kim, *Chem. Sci.* **2014**, *5*, 751.

26. Z. Wang, S. Chen, J. W. Y. Lam, W. Qin, R. T. K. Kwok, N. Xie, Q. Hu, B. Z. Tang, *J. Am. Chem. Soc.* **2013**, *135*, 8238.
27. D. D. La, S. V. Bhosale, L. A. Jones, S. V. Bhosale, *ACS Appl. Mater. Interface* **2018**, *10*, 12189.
28. J. Gierschner, J. Shi, B. Milián-Medina, D. Roca-Sanjuán, S. Varghese, S. Park, *Adv. Opt. Mater.* **2021**, *9*, 2002251.
29. S. Suzuki, S. Sasaki, A. S. Sairi, R. Iwai, B. Z. Tang, G.-i. Konishi, *Angew. Chem. Int. Ed.* **2020**, *59*, 9856.
30. R. Iwai, S. Suzuki, S. Sasaki, A. S. Sairi, K. Igawa, T. Suenobu, K. Morokuma, G.-i. Konishi, *Angew. Chem. Int. Ed.* **2020**, *59*, 10566.
31. S. Sasaki, K. Igawa, G.-i. Konishi, *J. Mater. Chem. C* **2015**, *3*, 5940.
32. S. Sasaki, S. Suzuki, W. M. C. Sameera, K. Igawa, K. Morokuma, G.-i. Konishi, *J. Am. Chem. Soc.* **2016**, *138*, 8194.
33. S. Sasaki, S. Suzuki, K. Igawa, K. Morokuma, G.-i. Konishi, *J. Org. Chem.* **2017**, *82*, 6865.
34. R. J. MacDonell, M. S. Schuurman, *Chem. Phys.* **2018**, *515*, 360.
35. J. Guan, R. Wei, A. Prlj, J. Peng, K.-H. Lin, J. Liu, H. Han, C. Corminboeuf, D. Zhao, Z. Yu, J. Zheng, *Angew. Chem. Int. Ed.* **2020**, *59*, 14903.
36. Q. Li, L. Blancafort, *Chem. Commun.* **2013**, *49*, 5966.
37. X.-L. Peng, S. Ruiz-Barragan, Z.-S. Li, Q.-S. Li, L. Blancafort, *J. Mater. Chem. C* **2016**, *4*, 2802.
38. A. Koch, D. Kinzel, F. Dröge, S. Gräfe, S. Kupfer, *J. Phys. Chem. C* **2017**, *121*, 16066.
39. M. F. S. J. Menger, F. Plasser, B. Mennucci, L. González, *J. Chem. Theory Comput.* **2018**, *14*, 6139.
40. J. Westermayr, M. Gastegger, M. F. S. J. Menger, S. Mai, L. González, P. Marquetand, *Chem. Sci.* **2019**, *10*, 8100.
41. L. Pan, H. Wu, J. Liu, K. Xue, W. Luo, P. Chen, Z. Wang, A. Qin, B. Z. Tang, *Adv. Opt. Mater.* **2019**, *7*, 1801673.
42. Q. Wan, J. Tong, B. Zhang, Y. Li, Z. Wang, B. Z. Tang, *Adv. Opt. Mater.* **2020**, *8*, 1901520.
43. Q. Peng, Y. Yi, Z. Shuai, J. Shao, *J. Am. Chem. Soc.* **2007**, *129*, 9333.
44. P.-A. Yin, Q. Wan, Y. Niu, Q. Peng, Z. Wang, Y. Li, A. Qin, Z. Shuai, B. Z. Tang, *Adv. Electron Mater.* **2020**, *6*, 2000255.
45. T. Zhang, Y. Jiang, Y. Niu, D. Wang, Q. Peng, Z. Shuai, *J. Phys. Chem. A* **2014**, *118*, 9094.
46. Q. Ou, Q. Peng, Z. Shuai, *J. Phys. Chem. Lett.* **2020**, *11*, 7790.
47. Z. Shuai, Q. Peng, *Phys. Rep.* **2014**, *537*, 123.
48. Z. Lin, A. W. Kohn, T. Van Voorhis, *J. Phys. Chem. C* **2020**, *124*, 3925.
49. N. Kuritz, T. Stein, R. Baer, L. Kronik, *J. Chem. Theory Comput.* **2011**, *7*, 2408.
50. R. Cammi, B. Mennucci, *J. Chem. Phys.* **1999**, *110*, 9877.
51. M. J. Field, P. A. Bash, M. Karplus, *J. Comput. Chem.* **1990**, *11*, 700.
52. Y. Shao, M. Head-Gordon, A. I. Krylov, *J. Chem. Phys.* **2003**, *118*, 4807.
53. Y. A. Bernard, Y. Shao, A. I. Krylov, *J. Chem. Phys.* **2012**, *136*, 204103.
54. Z. Shuai, *Chin. J. Chem.* **2020**, *38*, 1223.
55. Z. Shuai, Q. Peng, *Natl. Sci. Rev.* **2016**, *4*, 224.
56. Z. Liu, T. Lu, Q. Chen, *Carbon* **2020**, *165*, 461.
57. T. Lu, F. Chen, *J. Comput. Chem.* **2012**, *33*, 580.
58. J. M. Herbert, X. Zhang, A. F. Morrison, J. Liu, *Acc. Chem. Res.* **2016**, *49*, 931.
59. S. Lin, Q. Peng, Q. Ou, Z. Shuai, *Inorg. Chem.* **2019**, *58*, 14403.
60. W.-L. Ding, X.-L. Peng, G.-L. Cui, Z.-S. Li, L. Blancafort, Q.-S. Li, *ChemPhotoChem* **2019**, *3*, 814.
61. D. de Castro Araujo Valente, I. Borges, T. M. Cardozo, *Phys. Chem. Chem. Phys.* **2021**, *23*, 26561.
62. L. Stojanović, R. Crespo-Otero, *ChemPhotoChem* **2019**, *3*, 907.
63. L. Stojanović, R. Crespo-Otero, *J. Phys. Chem. C* **2020**, *124*, 17752.
64. L. Stojanović, R. Crespo-Otero, *Molecules* **2022**, *27*, 522.

SUPPORTING INFORMATION

Additional supporting information can be found online in the Supporting Information section at the end of this article.

How to cite this article: P.-A. Yin, Q. Ou, Q. Peng, Z. Shuai, *Aggregate* **2022**, e291. https://doi.org/10.1002/agt2.291